The SARS-CoV-2 conserved macrodomain is a mono-ADP-ribosylhydrolase

Yousef M.O. Alhammad[a], Maithri M. Kashipathy[b], Anuradha Roy[c], Jean-Philippe Gagné[d,e], Peter McDonald[c], Philip Gao[f], Louis Nonfoux[d,e], Kevin P. Battaile[g], David K. Johnson[h], Erik D. Holmstrom[a], Guy G. Poirier[d,e], Scott Lovell[b] and Anthony R. Fehr[a,#]

[a]Department of Molecular Biosciences, University of Kansas, Lawrence, Kansas 66045, USA
[b]Protein Structure Laboratory, University of Kansas, Lawrence, Kansas 66047, USA
[c]High Throughput Screening Laboratory, University of Kansas, Lawrence, Kansas 66047, USA
[d]Department of Molecular Biology, Medical Biochemistry and Pathology, Laval University Cancer Research Center, Québec City, QC, G1V 0A6, Canada
[e]CHU de Québec Research Center, CHUL Pavilion, Oncology Division, Québec City, QC, G1V 4G2, Canada
[f]Protein Production Group, University of Kansas, Lawrence, Kansas 66047, USA
[g]NYX, New York Structural Biology Center, Upton, NY 11973, USA
[h]Molecular Graphics and Modeling Laboratory and the Computational Chemical Biology Core, University of Kansas, Lawrence, Kansas 66047, USA

[#]Correspondence: arfehr@ku.edu; Tel.: +1- (785) 864-6626 (K.S.)

Running title: SARS-CoV-2 Mac1 removes ADP-ribose from protein

Keywords: Coronavirus, SARS-CoV-2, macrodomain, ADP-ribose, poly-ADP-ribose,

ABSTRACT

Severe acute respiratory syndrome coronavirus 2 (SARS-CoV-2) and other SARS-like-CoVs encode 3 tandem macrodomains within non-structural protein 3 (nsp3). The first macrodomain, Mac1, is conserved throughout CoVs, and binds to and hydrolyzes mono-ADP-ribose (MAR) from target proteins. Mac1 likely counters host-mediated anti-viral ADP-ribosylation, a posttranslational modification that is part of the host response to viral infections. Mac1 is essential for pathogenesis in multiple animal models of CoV infection, implicating it as a virulence factor and potential therapeutic target. Here we report the crystal structure of SARS-CoV-2 Mac1 in complex with ADP-ribose. SARS-CoV-2, SARS-CoV and MERS-CoV Mac1 exhibit similar structural folds and all 3 proteins bound to ADP-ribose with low μM affinities. Importantly, using ADP-ribose detecting binding reagents in both a gel-based assay and novel ELISA assays, we demonstrated de-MARylating activity for all 3 CoV Mac1 proteins, with the SARS-CoV-2 Mac1 protein leading to a more rapid loss of substrate compared to the others. In addition, none of these enzymes could hydrolyze poly-ADP-ribose. We conclude that the SARS-CoV-2 and other CoV Mac1 proteins are MAR-hydrolases with similar functions, indicating that compounds targeting CoV Mac1 proteins may have broad anti-CoV activity.

40 **IMPORTANCE**

41 SARS-CoV-2 has recently emerged into the human population and has led to a worldwide
42 pandemic of COVID-19 that has caused greater than 900 thousand deaths worldwide. With, no
43 currently approved treatments, novel therapeutic strategies are desperately needed. All
44 coronaviruses encode for a highly conserved macrodomain (Mac1) that binds to and removes
45 ADP-ribose adducts from proteins in a dynamic post-translational process increasingly
46 recognized as an important factor that regulates viral infection. The macrodomain is essential for
47 CoV pathogenesis and may be a novel therapeutic target. Thus, understanding its biochemistry
48 and enzyme activity are critical first steps for these efforts. Here we report the crystal structure of
49 SARS-CoV-2 Mac1 in complex with ADP-ribose, and describe its ADP-ribose binding and
50 hydrolysis activities in direct comparison to SARS-CoV and MERS-CoV Mac1 proteins. These
51 results are an important first step for the design and testing of potential therapies targeting this
52 unique protein domain.

53

54 **INTRODUCTION**

55 The recently emerged pandemic outbreak of COVID-19 is caused by a novel coronavirus
56 named severe acute respiratory syndrome coronavirus 2 (SARS-CoV-2) (1, 2). As of September
57 16, 2020, this virus has been responsible for ~ 30 million cases of COVID-19 and >900,000
58 deaths worldwide. SARS-CoV-2 is a member of the lineage B β-CoVs with overall high
59 sequence similarity with other SARS-like CoVs, including SARS-CoV. While most of the
60 genome is >80% similar with SARS-CoV, there are regions where amino acid conservation is
61 significantly lower. As expected, the most divergent proteins in the SARS-CoV-2 genome from
62 SARS-CoV include the Spike glycoprotein and several accessory proteins including 8a (absent),
63 8b (extended), and 3b (truncated). However, somewhat unexpectedly, several non-structural
64 proteins also show significant divergence from SARS-CoV, including non-structural proteins 3,
65 4, and 7, which could affect the biology of SARS-CoV-2 (3, 4).

66 Coronaviruses encode 16 non-structural proteins that are translated from two open
67 reading frames (ORFs), replicase 1a and 1ab (rep1a and rep1ab) (5). The largest non-structural
68 protein is the non-structural protein 3 (nsp3) that encodes for multiple modular protein domains.
69 These domains in SARS-CoV-2 diverge in amino acid sequence from SARS-CoV as much as
70 30%, and SARS-CoV-2 nsp3 includes a large insertion of 25-41 residues just upstream of the
71 first of three tandem macrodomains (Mac1, Mac2, and Mac3) (Fig. 1A) (3). In addition to this
72 insertion, the individual macrodomains show large amounts of amino acid divergence. Mac1
73 diverges 28% from SARS-CoV and 59% from MERS-CoV, while Mac2 and Mac3 diverge 24%
74 from SARS-CoV. It is feasible that these significant sequence differences could impact the
75 unique biology of SARS-CoV-2. However, macrodomains have a highly conserved structure,
76 and thus sequence divergence may have little impact on their overall function. Mac1 is present in

77 all CoVs, unlike Mac2 and Mac3, and early structural and biochemical data demonstrated that it
78 contains a conserved three-layered α/β/α fold and binds to mono-ADP-ribose (MAR) and other
79 related molecules (6-10). This is unlike Mac2 and Mac3, which fail to bind ADP-ribose and
80 instead appear to bind to nucleic acids (11, 12). ADP-ribose is buried in a hydrophobic cleft of
81 Mac1 where the ADP-ribose binds to several highly-conserved residues such as aspartic acid at
82 position 23 (D23) and asparagine at position 41 (N41) of SARS-CoV (Fig. 1B) (6). Mac1
83 homologs are also found in alphaviruses, Hepatitis E virus, and Rubella virus, and structural
84 analysis of these macrodomains have demonstrated that they are very similar to CoV Mac1 (13,
85 14). All are members of the larger MacroD-type macrodomain family, which includes human
86 macrodomains Mdo1 and Mdo2 (15).

87 The CoV Mac1 was originally named ADP-ribose-1”-phosphatase (ADRP) based on data
88 demonstrating that it could remove the phosphate group from ADP-ribose-1”-phosphate (6-8).
89 However, the activity was rather modest, and it was unclear why this would impact a virus
90 infection. More recently it has been demonstrated that CoV Mac1 can hydrolyze the bond
91 between amino acid chains and ADP-ribose molecules (16-18), indicating that it can reverse
92 protein ADP-ribosylation (6, 8). ADP-ribosylation is a post-translational modification catalyzed
93 by ADP-ribosyltransferases (ARTs, also known as PARPs) through transferring an ADP-ribose
94 moiety from NAD^+ onto target proteins (19). The ADP-ribose is transferred as a single unit of
95 MAR, or single units of MAR are transferred consecutively to form a PAR chain. Several Mac1
96 proteins have been shown to hydrolyze MAR, but have minimal activity towards PAR (16, 17).
97 Several MARylating PARPs are induced by interferon (IFN) and are known to inhibit virus
98 replication, implicating MARylation in the host-response to infection (20).

99 Several reports have addressed the role of Mac1 on the replication and pathogenesis of
100 CoVs, mostly using the mutation of a highly conserved asparagine to alanine (N41A-SARS-
101 CoV). This mutation abolished the MAR-hydrolase activity of SARS-CoV Mac1 (18). This
102 mutation has minimal effects on CoV replication in transformed cells, but reduces viral load,
103 leads to enhanced IFN production, and strongly attenuates both murine hepatitis virus (MHV)
104 and SARS-CoV in mouse models of infection (7, 18, 21, 22). MHV Mac1 was also required for
105 efficient replication in primary macrophages, which could be partially rescued by the PARP
106 inhibitors XAV-939 and 3-AB or siRNA knockdown of PARP12 or PARP14 (23). These data
107 suggest that Mac1's likely function is to counter PARP-mediated anti-viral ADP-ribosylation
108 (24). Mutations in the alphavirus and HEV macrodomain also have substantial phenotypic
109 effects on virus replication and pathogenesis (16, 25-28). As viral macrodomains are clearly
110 important virulence factors, they are considered to be potential targets for anti-viral therapeutics
111 (24).
112 Based on the close structural similarities between viral macrodomains, we hypothesized
113 that SARS-CoV-2 Mac1 has similar binding and hydrolysis activity as other CoV Mac1
114 enzymes. In this study, we determined the crystal structure of the SARS-CoV-2 Mac1 protein
115 bound to ADP-ribose. Binding to and hydrolysis of MAR was tested and directly compared to a
116 human macrodomain (Mdo2) and the SARS-CoV and MERS-CoV Mac1 proteins by several *in*
117 *vitro* assays. All CoV Mac1 proteins bound to MAR and could remove MAR from a protein
118 substrate. However, the initial rate associated with the loss of substrate was largest for the
119 SARS-CoV-2 Mac1 protein , especially under multi-turnover conditions. In addition, none of
120 these enzymes could remove PAR from a protein substrate. These results indicate that Mac1

121 protein domains likely have similar functions, and will be instrumental in the design and testing

122 of novel therapeutic agents targeting the CoV Mac1 protein domain.

123

124 **RESULTS**

125 **Structure of the SARS-CoV-2 Mac1 complexed with ADP-ribose.** To create recombinant
126 SARS-CoV-2 Mac1 for structure determination and enzyme assays, nucleotides 3348-3872 of
127 SARS-CoV-2 isolate Wuhan-hu-1 (accession number NC_045512), representing amino acids
128 I1023-K1197 of rep1a, were cloned into a bacterial expression vector containing an N-terminal
129 6X-His tag and TEV cleavage site. We obtained large amounts (>100 mg) of purified
130 recombinant protein (Fig. S1A). A small amount of this protein was digested by the TEV
131 protease to obtain protein devoid of any extra tags for crystallization and used to obtain crystals
132 from which the structure was determined (Fig. S1B). Our crystallization experiments resulted in
133 the same crystal form (needle clusters) from several conditions, but only when ADP-ribose was
134 added to the protein. This represents an additional crystal form ($P2_1$) amongst the recently
135 determined SARS-CoV-2 macrodomain structures (29-31).

136 The structure of SARS-CoV-2 Mac1 complexed with ADP-ribose was obtained using X-
137 ray diffraction data to 2.2 Å resolution and contained four molecules in the asymmetric unit that
138 were nearly identical. The polypeptide chains could be traced from V3-M171 for subunits A/C
139 and V3-K172 for subunits B/D. Superposition of subunits B-D onto subunit A (169 residues
140 aligned) yielded RMSD deviations of 0.17 Å, 0.17 Å and 0.18 Å respectively between Cα atoms.
141 As such, subunit A was used for the majority of the structure analysis described herein. The
142 SARS-CoV-2 Mac1 protein adopted a fold consistent with the MacroD sub-family of
143 macrodomains that contains a core composed of a mixed arrangement of 7 β-sheets (parallel and
144 antiparallel) that are flanked by 6 α-helices (Fig. 2A-B).

145 As mentioned above, apo crystals were never observed for our construct, though the apo
146 structure has been solved by researchers at The Center for Structural Genomics of Infectious

147 Diseases (PDB 6WEN) (30) and the University of Wisconsin-Milwaukee (PDB 6WEY) (32).
148 Further analysis of the amino acid sequences used for expression and purification revealed that
149 our construct had 5 additional residues at the C-terminus (MKSEK) and differs slightly at the N-
150 terminus as well (GIE vs GE) relative to 6WEN. In addition, the sequence used to obtain the
151 structure of 6WEY is slightly shorter than SARS-CoV-2 Mac1 at both the N and C-terminal
152 regions (Fig. S2A). To assess the effect of these additional residues on crystallization, chain B
153 of the SARS-CoV-2 Mac1, which was traced to residue K172, was superimposed onto subunit A
154 of PDB 6W02 (31), a previously determined structure of ADP-ribose bound SARS-CoV-2 Mac1.
155 Analysis of the crystal packing of 6W02 indicates that the additional residues at the C-terminus
156 would clash with symmetry related molecules (Fig. S2B). This suggests that the presence of
157 these extra residues at the C-terminus likely prevented the generation of the more tightly packed
158 crystal forms obtained for 6W02 and 6WEY, which diffracted to high resolution.
159 The ADP-ribose binding pocket contained large regions of positive electron density
160 consistent with the docking of ADP-ribose (Fig. 3A). The adenine forms two hydrogen bonds
161 with D22-I23, which makes up a small loop between β2 and the N-terminal half of α1. The side
162 chain of D22 interacts with N6, while the backbone nitrogen atom of I23 interacts with N1, in a
163 very similar fashion to the SARS-CoV macrodomain (6). This aspartic acid is known to be
164 critical for ADP-ribose binding for alphavirus macrodomains (26, 27). A large number of
165 contacts are made in the highly conserved loop between β3 and α2 which includes many highly-
166 conserved residues, including a GGG (motif) and N40, which is completely conserved in all
167 enzymatically active macrodomains (33). N40 is positioned to make hydrogen bonds with the 3'
168 OH groups of the distal ribose, as well as a conserved water molecule (Fig. 3B-C). K44 and G46
169 also make hydrogen bonds with the 2' OH of the distal ribose, G48 makes contact with the 1'

170 OH and a water that resides near the catalytic site, while the backbone nitrogen atom of V49
171 hydrogen bonds with the α-phosphate. The other major interactions with ADP-ribose occur in
172 another highly conserved region consisting of residues G130, I131, and F132 that are in the loop
173 between β6 and α5 (Fig. 3B). The α-phosphate accepts a hydrogen bond from the nitrogen atom
174 of I131, while the β-phosphate accepts hydrogen bonds from the backbone nitrogen atom of
175 G130 and F132. The phenyl ring of F132 may make van der Waals interactions with the distal
176 ribose to stabilize it, which may contribute to binding and hydrolysis (34). Loops β3-α2 and β6-
177 α5 are connected by an isoleucine bridge that forms a narrow channel around the diphosphate
178 which helps position the terminal ribose for water-mediated catalysis (6). Of all these residues, is
179 not exactly clear which ones are important for ADP-ribose binding, hydrolysis, or both.
180 Additionally, a network of direct contacts of ADP-ribose to solvent along with water mediated
181 contacts to the protein are shown (Fig. 3C).

182 **Comparison of SARS-CoV-2 Mac1 with other CoV macrodomain structures.** We
183 next sought to compare the SARS-CoV-2 Mac1 to other deposited structures of this protein.
184 Superposition with Apo (6WEN) and ADP-ribose complexed protein (6W02) yielded RMSD of
185 0.48 Å (168 residues) and 0.37 Å (165 residues), respectively, indicating a high degree of
186 similarity (Fig. S3A-B). Comparison of the ADP-ribose binding site of SARS-CoV-2 Mac1 with
187 that of the apo structure (6WEN) revealed minor conformational differences in order to
188 accommodate ADP-ribose binding. The loop between β3 and α2 (H45-V49) undergoes a change
189 in conformation and the sidechain of F132 is moved out of the ADP-ribose binding site (Fig.
190 S3C). Our ADP-ribose bound structure is nearly identical to 6W02, except for slight deviations
191 in the β3-α2 loop and an altered conformation of F156, where the aryl ring of F156 is moved
192 closer to the adenine ring (Fig. S3 C-D). However, this is likely a result of crystal packing as

193 F156 adopts this conformation in each subunit and would likely clash with subunit residues
194 related by either crystallographic or non-crystallographic symmetry.
195 We next compared the ADP-ribose bound SARS-CoV-2 Mac1 structure with that of
196 SARS-CoV (PDB 2FAV) (6) and MERS-CoV (PDB 5HOL) (35) Mac1 proteins. Superposition
197 yielded RMSD deviations of 0.71 Å (166 residues) and 1.06 Å (161 residues) for 2FAV and
198 5HOL, respectively. Additionally, the ADP-ribose binding mode in the SARS-CoV and SARS-
199 CoV-2 structures almost perfectly superimposed (Fig. 4A-D). The conserved aspartic acid
200 residue (D22, SARS-CoV-2) that binds to adenine, is localized in a similar region in all 3
201 proteins although there are slight differences in the rotamers about the Cβ-Cγ bond. The angles
202 between the mean planes defined by the OD1, CG and OD2 atoms relative to SARS-CoV-2
203 Mac1 is 23.1^{o} and 46.5^{o} for the SARS-CoV and MERS-CoV Mac1 structures, respectively.
204 Another notable difference is that SARS-CoV and SARS-CoV-2 macrodomains have an
205 isoleucine (I23) following this aspartic acid while MERS-CoV has an alanine (A22). Conversely,
206 SARS-CoV-2 and SARS-CoV Mac1 have a valine instead of an isoleucine immediately
207 following the GGG motif (V49/I48). From these structures it appears that having two isoleucines
208 in this location would clash, and that lineage B and lineage C β-CoVs has evolved in unique
209 ways to create space in this pocket (Fig. 4D and data not shown). Despite these small differences
210 in local structure, the overall structure of CoV Mac1 domains remain remarkably conserved, and
211 indicates they likely have similar biochemical activities and biological functions.
212 **SARS-CoV, SARS-CoV-2, and MERS-CoV bind to ADP-ribose with similar**
213 **affinities.** To determine if the CoV macrodomains had any noticeable differences in their ability
214 to bind ADP-ribose, we performed isothermal titration calorimetry (ITC), which measures the
215 energy released or absorbed during a binding reaction. Macrodomain proteins from human

216 (Mdo2), SARS-CoV, MERS-CoV, and SARS-CoV-2 were purified (Fig. S1A) and tested for
217 their affinity to ADP-ribose. All CoV Mac1 proteins bound to ADP-ribose with low micromolar
218 affinity (7-16 μM), while human Mdo2 bound with an affinity about 10-times stronger (~220
219 nM) (Fig. 5A-B). As a control we tested the ability of the MERS-CoV macrodomain to bind to
220 ATP, and only observed minimal binding with mM affinity (data not shown). At higher
221 concentrations, the SARS-CoV-2 macrodomain caused a slightly endothermic reaction,
222 potentially the result of protein aggregation or a change in conformation (Fig. 5A). The MERS-
223 CoV Mac1 had a greater affinity for ADP-ribose than SARS-CoV or SARS-CoV-2 Mac1 in the
224 ITC assay (Fig. 5A-B), however, our results found the differences between these macrodomain
225 proteins to be much closer than previously reported (9). As an alternate method to confirm ADP-
226 ribose binding, we conducted a thermal shift assay. All 4 macrodomains tested denatured at
227 higher temperatures with the addition of ADP-ribose (Fig. S4). We conclude that lineage B and
228 lineage C β-CoV Mac1 proteins bind to ADP-ribose with similar affinities.
229 **CoV macrodomains are MAR-hydrolases.** To examine the MAR-hydrolase activity of
230 CoV Mac1, we first tested the viability of using ADP-ribose binding reagents to detect
231 MARylated protein. Previously, radiolabeled NAD^+ has been the primary method used to label
232 MARylated protein (16, 17). To create a MARylated substrate, the catalytic domain of the
233 PARP10 (GST-PARP10 CD) protein was incubated with NAD^+, leading to its automodification.
234 PARP10 CD is a standard substrate that has been used extensively in the field to analyze the
235 activity of macrodomains (16, 18, 26, 27). PARP10 is highly upregulated upon CoV infection
236 (23, 36) and is known to primarily auto-MARylate itself on acidic residues, which are the targets
237 of the MacroD2 class of macrodomains (27). We then tested a panel of anti-MAR, anti-PAR, or
238 both anti-MAR and anti-PAR binding reagents/antibodies for the ability to detect MARylated

239 PARP10 by immunoblot. The anti-MAR and anti-MAR/PAR binding reagents, but not anti-PAR
240 antibody, bound to MARylated PARP10 (Fig. S5). Therefore, in this work we utilized the anti-
241 MAR binding reagent to detect MARylated PARP10.

242 We next tested the ability of SARS-CoV-2 Mac1 to remove ADP-ribose from
243 MARylated PARP10. SARS-CoV-2 Mac1 and MARylated PARP10 were incubated at
244 equimolar amounts of protein at 37ºC and the reaction was stopped at 5, 10, 20, 30, 45 or 60
245 minutes (Fig. 6A). As a control, MARylated PARP10 was incubated alone at 37ºC and collected
246 at similar time points (Fig. 6A and Fig. S6). Each reaction had equivalent amounts of
247 MARylated PARP10 and Mac1 which was confirmed by Coomassie Blue staining (Fig. 6A). An
248 immediate reduction of more than 50% band intensity was observed within five minutes, and the
249 ADP-ribose modification was nearly completely removed by SARS-CoV-2 Mac1 within 30
250 minutes (Fig. 6A). The MARylated PAPR10 bands intensities were calculated, plotted, and were
251 fit using non-linear regression (Fig. 6B). This result indicates that the SARS-CoV-2 Mac1
252 protein is a mono-ADP-ribosylhydrolase enzyme.

253 Next, we compared the MAR-hydrolase activity of Mac1 proteins from SARS-CoV-2,
254 SARS-CoV, and MERS-CoV and human (i.e., Mdo2). Specifically, we monitored the time-
255 dependent loss of substrate using immunoblotting (Fig. 6C) under equimolar (i.e., 1 μM
256 [Mac1]:1 μM [substrate]) and multiple-turnover conditions (i.e., 0.5 μM [substrate]:0.1 μM
257 [Mac1] and 1.0 μM [substrate]:0.1 μM [Mac1]), with total protein amounts confirmed by
258 Coomassie blue staining (Fig. S7). The resulting substrate decay plots (Fig. 6D) were fit using
259 non-linear regression to determine the initial rate (*k*) of substrate decay. Our results indicate that
260 the three CoV Mac1 proteins give rise to similar, but not identical, values of *k* (Fig. 6D). The
261 SARS-CoV-2 Mac1 protein has a greater *k* than the SARS-CoV or MERS-CoV Mac1 proteins,

262 especially under multiple-turnover conditions, and all 3 viral macrodomains gave rise to a more
263 rapid loss of substrate than the human Mdo2 enzyme (Fig. 6F). However, further enzymatic
264 analyses of these proteins are warranted to more thoroughly understand their kinetics and
265 binding affinities associated with various MARylated substrates.

266 **CoV Mac1 proteins do not hydrolyze PAR.** To determine if the CoV Mac1 proteins
267 could remove PAR from proteins, we incubated these proteins with an auto-PARylated PARP1
268 protein. PARP1 was incubated with increasing concentrations of NAD^+ to create a range of
269 modification levels (Fig. S8). We incubated both partially and heavily modified PARP1 with all
270 four macrodomains and PARG as a positive control for 1 hour. While PARG completely
271 removed PAR, none of the macrodomain proteins removed PAR chains from PARP1 (Fig. 7).
272 We conclude that macrodomain proteins are unable to remove PAR from an automodified
273 PARP1 protein under these conditions.

274 **ELISA assays can be used to measure ADP-ribosylhydrolase activity of**
275 **macrodomains.** Gel based assays as described above suffer from significant limitations in the
276 number of samples that can be done at once. A higher throughput assay will be needed to more
277 thoroughly investigate the activity of these enzymes and to screen for inhibitor compounds.
278 Based on the success of our antibody-based detection of MAR, we developed an ELISA assay
279 that has a similar ability to detect de-MARylation as our gel-based assay, but with the ability to
280 do so in a higher throughput manner (Fig. 8A). First, MARylated PARP10 was added to ELISA
281 plates. Next, the wells were washed and then incubated with different concentrations of the
282 SARS-CoV-2 Mac1 protein for 60 min. After incubation, the wells were washed and treated with
283 anti-MAR binding reagent, followed by HRP-conjugated secondary antibody and the detection
284 reagent. As controls, we detected MARylated and non-MARylated PARP10 proteins bound to

285 glutathione plates with anti-GST antibody and anti-MAR binding reagents and their
286 corresponding secondary antibodies (Fig. 8B). SARS-CoV-2 Mac1 was able to remove MAR
287 signal in a dose-dependent manner and plotted to a linear non-regression fitted line (Fig. 8C).
288 Based on these results, we believe that this ELISA assay will be a useful tool for screening
289 potential inhibitors of macrodomain proteins.

290 **DISCUSSION**

291 Here we report the crystal structure of SARS-CoV-2 Mac1 and its enzyme activity *in*
292 *vitro*. Structurally, it has a conserved three-layered α/β/α fold typical of the MacroD family of
293 macrodomains, and is extremely similar to other CoV Mac1 proteins (Fig. 2-4). The conserved
294 CoV macrodomain (Mac1) was initially described as an ADP-ribose-1”-phosphatase (ADRP), as
295 it was shown to be structurally similar to yeast enzymes that have this enzymatic activity (37).
296 Early biochemical studies confirmed this activity for CoV Mac1, though its phosphatase activity
297 for ADP-ribose-1”-phosphate was rather modest (6-8). Later, it was shown that mammalian
298 macrodomain proteins could remove ADP-ribose from protein substrates, indicating protein de-
299 ADP-ribosylation as a more likely function for the viral macrodomains (33, 38, 39). Shortly
300 thereafter, the SARS-CoV, hCoV-229E, FIPV, several alphavirus, and the hepatitis E virus
301 macrodomains were demonstrated to have de-ADP-ribosylating activity (16-18). However, this
302 activity has not yet been reported for the MERS-CoV or SARS-CoV-2 Mac1 protein.

303 In this study, we show that the Mac1 proteins from SARS-CoV, MERS-CoV and SARS-
304 CoV-2 hydrolyze MAR from a protein substrate (Fig. 6). Their enzymatic activities were similar
305 despite sequence divergence of almost 60% between SARS-CoV-2 and MERS-CoV. However,
306 the initial rate associated with the loss of substrate was largest for the SARS-CoV-2 Mac1
307 protein, particularly under multiple-turnover conditions. It is unclear what structural or sequence
308 differences may account for the increased activity of the SARS-CoV-2 Mac1 protein under these
309 conditions, especially considering the pronounced structurally similarities between these
310 proteins, specifically the SARS-CoV Mac1 (0.71 Å RMSD). It is also unclear if these differences
311 would matter in the context of the virus infection, as the relative concentrations of Mac1 and its
312 substrate during infection is not known. We also compared these activities to the human Mdo2

313 macrodomain. Mdo2 had a greater affinity for ADP-ribose than the viral enzymes, but had
314 significantly reduced enzyme activity in our experiments. Due to its high affinity for ADP-
315 ribose, it is possible that the Mdo2 protein was partially inhibited by rebinding to the MAR
316 product in these assays. Regardless, these results suggest that the human and viral proteins likely
317 have structural differences that alter their biochemical activities *in vitro*, indicating that it may be
318 possible to create viral macrodomain inhibitors that don't impact the human macrodomains. We
319 also compared the ability of these macrodomain proteins to hydrolyze PAR. None of the
320 macrodomains were able to hydrolyze either partially or heavily modified PARP1, further
321 demonstrating that the primary enzymatic activity of these proteins is to hydrolyze MAR (Fig.
322 7).

323 When analyzing viral macrodomain sequences, it is clear that they have at least 3 highly
324 conserved regions (Fig. 1B)(24). The first region includes the NAAN (37-40) and GGG (residues
325 46-48) motifs in the loop between β3 and α2. The second domain includes a GIF (residues 130-
326 132) motif in the loop between β6 and α5. The final conserved region is a VGP (residues 96-98)
327 motif at the end of β5 and extends into the loop between β5 and α4. Both of the first two
328 domains have well defined interactions with ADP-ribose (Fig. 3). However, no one has
329 addressed the role of the VGP residues, though our structure indicates that the glycine may
330 interact with a water molecule that makes contact with the β-phosphate. Identifying residues that
331 directly contribute to ADP-ribose binding, hydrolysis, or both by CoV Mac1 proteins will be
332 critical to determining the specific roles of ADP-ribose binding and hydrolysis in CoV
333 replication and pathogenesis.

334 While all previous studies of macrodomain de-ADP-ribosylation have primarily used
335 radiolabeled substrate, we obtained highly repeatable and robust data utilizing ADP-ribose

336 binding reagents designed to specifically recognize MAR (40, 41). The use of these binding
337 reagents should enhance the feasibility of this assay for many labs that are not equipped for
338 radioactive work. Utilizing these binding reagents, we further developed an ELISA assay for de-
339 MARylation that has the ability to dramatically increase the number of samples that can be
340 analyzed compared to the gel-based assay. To our knowledge, previously developed ELISA
341 assays were used to measure ADP-ribosyltransferase activities (42) but no ELISA has been
342 established to test the ADP-ribosylhydrolase activity of macrodomain proteins. This ELISA
343 assay should be useful to those in the field to screen compounds for macrodomain inhibitors that
344 could be either valuable research tools or potential therapeutics.

345 The functional importance of the CoV Mac1 domain has been demonstrated in several
346 reports, mostly utilizing the mutation of a highly conserved asparagine that mediates contact with
347 the distal ribose (Fig. 3B) (18, 21, 22). However, the physiological relevance of Mac1 during
348 SARS-CoV-2 infection has yet to be determined. In addition, the proteins that are targeted by the
349 CoV Mac1 for de-ADP-ribosylation remains unknown. Unfortunately, there are no known
350 compounds that inhibit this domain that could help identify the functions of this protein during
351 infection. The outbreak of COVID-19 has illustrated an urgent need for developing multiple
352 therapeutic drugs targeting conserved coronavirus proteins. Mac1 appears to be an ideal
353 candidate for further drug development based on: *i)* its highly conserved structure and
354 biochemical activities within CoVs; and *ii)* its importance for multiple CoVs to cause disease.
355 Targeting Mac1 may also have the benefit of enhancing the innate immune response, as we have
356 shown that Mac1 is required for some CoVs to block IFN production (18, 23). Considering that
357 Mac1 proteins from divergent αCoVs such as 229E and FIPV also have de-ADP-ribosylating
358 activity (16, 17), it is possible that compounds targeting Mac1 could prevent disease caused by

359 of wide variety of CoV, including those of veterinary importance like porcine epidemic diarrhea
360 virus (PEDV). Additionally, compounds that inhibit Mac1 in combination with the structure
361 could help identify the mechanisms it uses to bind to its biologically relevant protein substrates,
362 remove ADP-ribose from these proteins, and potentially define the precise function for Mac1 in
363 SARS-CoV-2 replication and pathogenesis. In conclusion, the results described here will be
364 critical for the design and development of highly-specific Mac1 inhibitors that could be used
365 therapeutically to mitigate COVID-19 or future CoV outbreaks.
366

367 **METHODS**

368 **Plasmids**

369 The SARS-CoV macrodomain (Mac1) (residues 1000-1172 of pp1a) was cloned into the
370 pET21a+ expression vector with an N-terminal His tag. The MERS-CoV Mac1 (residues 1110-
371 1273 of pp1a) was also cloned into pET21a+ with a C-terminal His tag. SARS-CoV-2 Mac1
372 (residues 1023-1197 of pp1a) was cloned into the pET30a+ expression vector with an N-terminal
373 His tag and a TEV cleavage site (Synbio). The pETM-CN Mdo2 Mac1 (residues 7-243)
374 expression vector with an N-terminal His-TEV-V5 tag and the pGEX4T-PARP10-CD (residues
375 818-1025) expression vector with an N-terminal GST tag were previously described (33). All
376 plasmids were confirmed by restriction digest, PCR, and direct sequencing.

377 **Protein Expression and Purification**

378 A single colony of *E. coli* cells (C41(DE3)) containing plasmids harboring the constructs
379 of the macrodomain proteins was inoculated into 10 mL LB media and grown overnight at 37°C
380 with shaking at 250 rpm. The overnight culture was transferred to a shaker flask containing 2X
381 1L TB media at 37ºC until the OD600 reached 0.7. The proteins were either induced with 0.4
382 mM IPTG at 37ºC for 3 hours, or 17°C for 20 hours. Cells were pelleted at 3500 × g for 10 min
383 and frozen at -80°C. Frozen cells were thawed at room temperature, resuspended in 50 mM Tris
384 (pH 7.6), 150 mM NaCl, and sonicated using the following cycle parameters: Amplitude: 50%,
385 Pulse length: 30 seconds, Number of pulses: 12, while incubating on ice for >1min between
386 pulses. The soluble fraction was obtained by centrifuging the cell lysate at 45,450 × g for 30
387 minutes at 4°C. The expressed soluble proteins were purified by affinity chromatography using
388 a 5 ml prepacked HisTrap HP column on an AKTA Pure protein purification system (GE
389 Healthcare). The fractions were further purified by size-exclusion chromatography (SEC) with a

390 Superdex 75 10/300 GL column equilibrated with 20mM Tris (pH 8.0), 150 mM NaCl and the
391 protein sized as a monomer relative to the column calibration standards. To cleave off the His tag
392 from the SARS-CoV-2 Mac1, purified TEV protease was added to purified SARS-CoV-2 Mac1
393 protein at a ratio of 1:10 (w/w), and then passed back through the Ni-NTA HP column. Protein
394 was collected in the flow through and equilibrated with 20 mM Tris (pH 8.0), 150 mM NaCl.
395 The SARS-CoV-2 Mac1, free from the N-terminal 6X-His tag, was used for subsequent
396 crystallization experiments.
397 For the PARP10-CD protein, the cell pellet was resuspended in 50 mM Tris-HCl (pH
398 8.0), 500 mM NaCl, 0.1mM EDTA, 25% glycerol, 1 mM DTT and sonicated as described above.
399 The cell lysate was incubated with 10 ml of Glutathione Sepharose 4B resin from GE Healthcare,
400 equilibrated with the same buffer for 2 hours, then applied to a gravity flow column to allow
401 unbound proteins to flow through. The column was washed with the resuspension buffer till the
402 absorbance at 280 nm reached baseline. The bound protein was eluted out of the column with
403 resuspension buffer containing 20 mM reduced glutathione and then dialyzed back into the
404 resuspension buffer overnight at 4°C.
405 **Isothermal Titration Calorimetry**
406 All ITC titrations were performed on a MicroCal PEAQ-ITC instrument (Malvern
407 Pananalytical Inc., MA). All reactions were performed in 20 mM Tris pH 7.5, 150 mM NaCl
408 using 100 μM of all macrodomain proteins at 25°C. Titration of 2 mM ADP-ribose or ATP
409 (MilliporeSigma) contained in the stirring syringe included a single 0.4 μL injection, followed by
410 18 consecutive injections of 2 μL. Data analysis of thermograms was analyzed using one set of
411 binding sites model of the MicroCal ITC software to obtain all fitting model parameters for the
412 experiments.

413 **Differential Scanning Fluorimetry (DSF)**

414 Thermal shift assay with DSF involved use of LightCycler® 480 Instrument (Roche
415 Diagnostics). In total, a 15 µL mixture containing 8X SYPRO Orange (Invitrogen), and 10 µM
416 macrodomain protein in buffer containing 20 mM Hepes, NaOH, pH 7.5 and various
417 concentrations of ADP-ribose were mixed on ice in 384-well PCR plate (Roche). Fluorescent
418 signals were measured from 25 to 95 °C in 0.2 °C/30-s steps (excitation, 470-505 nm; detection,
419 540-700 nm). The main measurements were carried out in triplicate. Data evaluation and Tm
420 determination involved use of the Roche LightCycler® 480 Protein Melting Analysis software,
421 and data fitting calculations involved the use of single site binding curve analysis on Graphpad
422 Prism.

423 **MAR Hydrolase Assays**

424 *Automodification of PARP10-CD protein*: A 10 µM solution of purified PAPR10-CD
425 protein was incubated for 20 minutes at 37ºC with 1 mM final concentration of β-Nicotinamide
426 Adenine Dinucleotide (β NAD^+) (Millipore-Sigma) in a reaction buffer (50 mM HEPES, 150
427 mM NaCl, 0.2 mM DTT, and 0.02% NP-40). MARylated PARP10 was aliquoted and stored at -
428 80ºC.

429 *PAPR10-CD ADP-ribose hydrolysis:* All reactions were performed at 37ºC for the
430 designated time. A 1 µM solution of MARylated PARP10-CD and purified Mac1 protein was
431 added in the reaction buffer (50 mM HEPES, 150 mM NaCl, 0.2 mM DTT, and 0.02% NP-40).
432 The reaction was stopped with addition of 2X Laemmli sample buffer containing 10% β-
433 mercaptoethanol.

434 Protein samples were heated at 95ºC for 5 minutes before loading and separated onto
435 SDS-PAGE cassette (Thermo Fisher Scientific Bolt™ 4-12% Bis-Tris Plus Gels) in MES

436 running buffer. For direct protein detection, the SDS-PAGE gel was stained using InstantBlue®
437 Protein Stain (Expedeon). For immunoblotting, the separated proteins were transferred onto
438 polyvinylidene difluoride (PVDF) membrane using iBlot™ 2 Dry Blotting System
439 (ThermoFisher Scientific). The blot was blocked with 5% skim milk in PBS containing 0.05%
440 Tween-20 and probed with anti-mono or poly ADP-ribose binding reagents/antibodies
441 MABE1076 (α-MAR), MABC547 (α-PAR), MABE1075 (α-MAR/PAR) (Millipore-Sigma) and
442 anti-GST tag monoclonal antibody MA4-004 (ThermoFisher Scientific). The primary antibodies
443 were detected with secondary infrared anti-rabbit and anti-mouse antibodies (LI-COR
444 Biosciences). All immunoblots were visualized using Odyssey® CLx Imaging System (LI-COR
445 Biosciences). The images were quantitated using Image J (National Institutes for Health (NIH))
446 or Image Studio software.

447 *Kinetic analysis of ADP-ribose hydrolysis:* To quantify the initial rate (k) of substrate
448 decay associated with the four macrodomains, each data set represented in the substrate decay
449 immunoblots in Fig. 6C, were fitted to a decaying exponential with the following functional
450 form: $([S]_{initial}-[S]_{final})e^{(-[k/[S]_{initial})t]}+[S]_{final}$ (Mathematica 12, Wolfram Alpha). The decay plots
451 and resulting values for the fitted parameter k along with statistic uncertainty (SD) are shown in
452 Fig. 6D.

453 *ELISA-based MAR hydrolysis:* ELISA Well-Coated™ Glutathione plates (G-Biosciences,
454 USA) were washed with phosphate-buffered saline (PBS) containing 0.05% Tween-20 (PBS-T)
455 and incubated with 50 µL of 100 nM automodified MARylated PARP10-CD in PBS for one
456 hour under room temperature. Following four washes with PBS-T, variable concentrations of
457 SARS-CoV-2 Mac1 were incubated with MARylated PARP10-CD for 60 minutes at 37ºC.
458 Purified macrodomains were 2-fold serially diluted starting at 100 nM in reaction buffer prior to

459 addition to MARylated PARP10-CD. Subsequently, ELISA wells were washed four times with
460 PBS-T and incubated with 50 µL/well of anti-GST (Invitrogen MA4-004) or anti-MAR
461 (Millipore-Sigma MAB1076) diluted 1:5,000 in 5 mg/ml BSA in PBS-T (BSA5-PBS-T) for 1
462 hour at room temperature. After four additional washes with PBS-T, each well was incubated
463 with 50 µL diluted 1:5,000 in BSA5-PBS-T of anti-rabbit-HRP (SouthernBiotech, USA) or anti-
464 mouse-HRP (Rockland Immunochemicals, USA) conjugate for 1 hour at room temperature. The
465 plate was washed four times with PBS-T and 100 µL of TMB peroxidase substrate solution
466 (SouthernBiotech, USA) was added to each well and incubated for 10 minutes. The peroxidase
467 reaction was stopped with 50 µL per well of 1 M HCl before proceeding to reading. Absorbance
468 was measured at 450 nm and subtracted from 620 nm using Biotek Powerwave XS plate reader
469 (BioTek). As controls, MARylated PARP10-CD and non-MARylated PARP10 were detected
470 with both anti-MAR and anti-GST antibodies. The absorbance of non-MARylated PARP10-CD
471 detected with anti-MAR antibody was used to establish the background signal. The % signal
472 remaining was calculated by dividing the experimental signal (+ enzyme) minus background by
473 the control (no enzyme) minus the background.

474 **PAR Hydrolase Assay**

475 *Automodification of PARP1 protein*: PARP1 was incubated with increasing
476 concentrations of NAD^+ to generate a range of PARP1 automodification levels. Highly purified
477 human 6X-His-PARP1 (43) (5 µg) was incubated for 30 min at 30°C in a reaction buffer
478 containing 100 mM Tris-HCl pH 8.0, 10 mM $MgCl_2$, 10% (v/v) glycerol, 10 mM DTT, 0 to 500
479 µM NAD+, 10% (v/v) ethanol and 25 µg/mL calf thymus activated DNA (Sigma-Aldrich).

480 *PARP1 ADP-ribose hydrolysis:* To evaluate the PAR hydrolase activity of CoV
481 macrodomains, 200 ng of slightly automodified PARP1 with 5 µM NAD^+ or highly

482 automodified with 500 μM NAD^+ were used as substrates for the de-PARylation assays.
483 Recombinant macrodomain protein (1 μg) was supplemented to the reaction buffer (100 mM
484 Tris-HCl pH 8.0, 10% (v/v) glycerol and 10 mM DTT) containing automodified PARP1 and
485 incubated for 1 hour at 37°C. Recombinant PARG (1 μg) was used as a positive control for PAR
486 erasing (44). Reaction mixtures were resolved on 4–12% Criterion™ XT Bis-Tris protein gels,
487 transferred onto nitrocellulose membrane and probed with the anti-PAR polyclonal antibody 96-
488 10.

489 **Structure Determination**

490 *Crystallization and Data Collection*: Purified SARS-CoV-2 Mac1 in 150 mM NaCl, 20
491 mM Tris pH 8.0 was concentrated to 13.8 mg/mL for crystallization screening. All crystallization
492 experiments were setup using an NT8 drop-setting robot (Formulatrix Inc.) and UVXPO MRC
493 (Molecular Dimensions) sitting drop vapor diffusion plates at 18°C. 100 nL of protein and 100
494 nL crystallization solution were dispensed and equilibrated against 50 μL of the latter. The
495 SARS-CoV-2 Mac1 complex with ADP-ribose was prepared by adding the ligand, from a 100
496 mM stock in water, to the protein at a final concentration of 2 mM. Crystals that were obtained in
497 1-2 days from the Salt Rx HT screen (Hampton Research) condition E10 (1.8 M
498 NaH_2PO_4/K_2HPO_4, pH 8.2). Refinement screening was conducted using the additive screen HT
499 (Hampton Research) by supplementing 10% of each additive to the Salt Rx HT E10 condition in
500 a new 96-well UVXPO crystallization plate. The crystals used for data collection were obtained
501 from Salt Rx HT E10 supplemented with 0.1 M NDSB-256 from the additive screen (Fig. S1).
502 Samples were transferred to a fresh drop composed of 80% crystallization solution and 20%
503 (v/v) PEG 200 and stored in liquid nitrogen. X-ray diffraction data were collected at the

504 Advanced Photon Source, IMCA-CAT beamline 17-ID using a Dectris Eiger 2X 9M pixel array
505 detector.

506 *Structure Solution and Refinement*: Intensities were integrated using XDS (45, 46) via
507 Autoproc (47) and the Laue class analysis and data scaling were performed with Aimless (48).
508 Notably, a pseudo-translational symmetry peak was observed at (0, 0.31 0.5) that was 44.6% of
509 the origin. Structure solution was conducted by molecular replacement with Phaser (49) using a
510 previously determined structure of ADP-ribose bound SARS-CoV-2 Mac1 (PDB 6W02) as the
511 search model. The top solution was obtained in the space group $P2_1$ with four molecules in the
512 asymmetric unit. Structure refinement and manual model building were conducted with Phenix
513 (50) and Coot (51) respectively. Disordered side chains were truncated to the point for which
514 electron density could be observed. Structure validation was conducted with Molprobity (52) and
515 figures were prepared using the CCP4MG package (53). Superposition of the macrodomain
516 structures was conducted with GESAMT (54).

517 **Statistical Analysis**

518 All statistical analyses were done using an unpaired two-tailed student's t-test to assess
519 differences in mean values between groups, and graphs are expressed as mean ±SD. Significant p
520 values are denoted with *$p \leq 0.05$.

521 **ACCESSION CODES**

522 The coordinates and structure factors for SARS-CoV-2 Mac1 were deposited to the
523 Worldwide Protein Databank (wwPDB) with the accession code 6WOJ.

524 **ACKNOWLEDGEMENTS**

525 We'd like to thank Ivan Ahel and Gytis Jankevicius (Oxford University) for providing
526 protein expression plasmids; John Pascal (University of Montreal) and Marie-France Langelier

527 (Universite de Montreal) for providing PARP1; and Wenqing Xu (University of Washington) for
528 providing PARG. This research was funded by the National Institutes of Health (NIH) grant
529 numbers P20 GM113117, P30GM110761, and AI134993-01, and University of Kansas start-up
530 funds to A.R.F, and the Canadian Institutes of Health Research grant number MOP-418863 to
531 G.G.P. Use of the IMCA-CAT beamline 17-ID at the Advanced Photon Source was supported by
532 the companies of the Industrial Macromolecular Crystallography Association through a contract
533 with Hauptman-Woodward Medical Research Institute. Use of the Advanced Photon Source was
534 supported by the U.S. Department of Energy, Office of Science, Office of Basic Energy
535 Sciences, under Contract No. DE-AC02-06CH11357.
536

537 **AUTHOR CONTRIBUTIONS**

538 Conceptualization: ARF, YMOA, GGP

539 Data curation: YMOA, SL, JPG, ARF, EDH

540 Formal analysis: YMOA, DKJ, AR, SL, ARF, EDH

541 Funding acquisition: GGP, SL, ARF

542 Investigation: YMOA, MMK, AR, JPG, LN, PM, KPB

543 Methodology: YMOA, GGP, AR, JPG, EDH, SL, ARF

544 Project administration: GGP, SL, ARF

545 Resources: AR, SL, PG, ARF

546 Supervision: AR, GGP, SL ARF

547 Validation: YMOA, SL, AR, JPG, GGP, ARF

548 Visualization: YMOA, ARF, AR, SL, JPG

549 Writing – original draft: YMOA, SL, ARF

550 Writing – review & editing: all authors

551

552 **REFERENCES**
553

554 1. Zhou P, Yang XL, Wang XG, Hu B, Zhang L, Zhang W, Si HR, Zhu Y, Li B, Huang CL,
555 Chen HD, Chen J, Luo Y, Guo H, Jiang RD, Liu MQ, Chen Y, Shen XR, Wang X, Zheng
556 XS, Zhao K, Chen QJ, Deng F, Liu LL, Yan B, Zhan FX, Wang YY, Xiao GF, Shi ZL.
557 2020. A pneumonia outbreak associated with a new coronavirus of probable bat origin.
558 Nature 579:270-273.
559 2. Coronaviridae Study Group of the International Committee on Taxonomy of V. 2020.
560 The species Severe acute respiratory syndrome-related coronavirus: classifying 2019-
561 nCoV and naming it SARS-CoV-2. Nat Microbiol 5:536-544.
562 3. Srinivasan S, Cui H, Gao Z, Liu M, Lu S, Mkandawire W, Narykov O, Sun M, Korkin D.
563 2020. Structural Genomics of SARS-CoV-2 Indicates Evolutionary Conserved
564 Functional Regions of Viral Proteins. Viruses 12:360.
565 4. Wu C, Liu Y, Yang Y, Zhang P, Zhong W, Wang Y, Wang Q, Xu Y, Li M, Li X, Zheng
566 M, Chen L, Li H. 2020. Analysis of therapeutic targets for SARS-CoV-2 and discovery
567 of potential drugs by computational methods. Acta Pharm Sin B
568 doi:10.1016/j.apsb.2020.02.008.
569 5. Fehr AR, Perlman S. 2015. Coronaviruses: An Overview of Their Replication and
570 Pathogenesis, p 1-23. *In* Maier HJ, Bickerton E, Britton P (ed), Coronaviruses, vol 1282.
571 Springer New York.
572 6. Egloff MP, Malet H, Putics A, Heinonen M, Dutartre H, Frangeul A, Gruez A,
573 Campanacci V, Cambillau C, Ziebuhr J, Ahola T, Canard B. 2006. Structural and
574 functional basis for ADP-ribose and poly(ADP-ribose) binding by viral macro domains. J
575 Virol 80:8493-502.
576 7. Putics A, Filipowicz W, Hall J, Gorbalenya AE, Ziebuhr J. 2005. ADP-ribose-1"-
577 monophosphatase: a conserved coronavirus enzyme that is dispensable for viral
578 replication in tissue culture. J Virol 79:12721-31.
579 8. Saikatendu KS, Joseph JS, Subramanian V, Clayton T, Griffith M, Moy K, Velasquez J,
580 Neuman BW, Buchmeier MJ, Stevens RC, Kuhn P. 2005. Structural basis of severe acute
581 respiratory syndrome coronavirus ADP-ribose-1"-phosphate dephosphorylation by a
582 conserved domain of nsP3. Structure 13:1665-75.
583 9. Cho CC, Lin MH, Chuang CY, Hsu CH. 2016. Macro Domain from Middle East
584 Respiratory Syndrome Coronavirus (MERS-CoV) Is an Efficient ADP-ribose Binding
585 Module: CRYSTAL STRUCTURE AND BIOCHEMICAL STUDIES. J Biol Chem
586 291:4894-902.
587 10. Xu Y, Cong L, Chen C, Wei L, Zhao Q, Xu X, Ma Y, Bartlam M, Rao Z. 2009. Crystal
588 structures of two coronavirus ADP-ribose-1"-monophosphatases and their complexes
589 with ADP-Ribose: a systematic structural analysis of the viral ADRP domain. J Virol
590 83:1083-92.
591 11. Tan J, Vonrhein C, Smart OS, Bricogne G, Bollati M, Kusov Y, Hansen G, Mesters JR,
592 Schmidt CL, Hilgenfeld R. 2009. The SARS-unique domain (SUD) of SARS coronavirus
593 contains two macrodomains that bind G-quadruplexes. PLoS Pathog 5:e1000428.
594 12. Chatterjee A, Johnson MA, Serrano P, Pedrini B, Joseph JS, Neuman BW, Saikatendu K,
595 Buchmeier MJ, Kuhn P, Wuthrich K. 2009. Nuclear magnetic resonance structure shows
596 that the severe acute respiratory syndrome coronavirus-unique domain contains a
597 macrodomain fold. J Virol 83:1823-36.

598 13. Makrynitsa GI, Ntonti D, Marousis KD, Birkou M, Matsoukas MT, Asami S, Bentrop D,
599 Papageorgiou N, Canard B, Coutard B, Spyroulias GA. 2019. Conformational plasticity
600 of the VEEV macro domain is important for binding of ADP-ribose. J Struct Biol
601 206:119-127.
602 14. Malet H, Coutard B, Jamal S, Dutartre H, Papageorgiou N, Neuvonen M, Ahola T,
603 Forrester N, Gould EA, Lafitte D, Ferron F, Lescar J, Gorbalenya AE, de Lamballerie X,
604 Canard B. 2009. The crystal structures of Chikungunya and Venezuelan equine
605 encephalitis virus nsP3 macro domains define a conserved adenosine binding pocket. J
606 Virol 83:6534-45.
607 15. Rack JG, Perina D, Ahel I. 2016. Macrodomains: Structure, Function, Evolution, and
608 Catalytic Activities. Annu Rev Biochem 85:431-54.
609 16. Li C, Debing Y, Jankevicius G, Neyts J, Ahel I, Coutard B, Canard B. 2016. Viral Macro
610 Domains Reverse Protein ADP-Ribosylation. J Virol 90:8478-86.
611 17. Eckei L, Krieg S, Butepage M, Lehmann A, Gross A, Lippok B, Grimm AR, Kummerer
612 BM, Rossetti G, Luscher B, Verheugd P. 2017. The conserved macrodomains of the non-
613 structural proteins of Chikungunya virus and other pathogenic positive strand RNA
614 viruses function as mono-ADP-ribosylhydrolases. Sci Rep 7:41746.
615 18. Fehr AR, Channappanavar R, Jankevicius G, Fett C, Zhao J, Athmer J, Meyerholz DK,
616 Ahel I, Perlman S. 2016. The Conserved Coronavirus Macrodomain Promotes Virulence
617 and Suppresses the Innate Immune Response during Severe Acute Respiratory Syndrome
618 Coronavirus Infection. mBio 7:e01721-16.
619 19. Kim DS, Challa S, Jones A, Kraus WL. 2020. PARPs and ADP-ribosylation in RNA
620 biology: from RNA expression and processing to protein translation and proteostasis.
621 Genes Dev 34:302-320.
622 20. Fehr AR, Singh SA, Kerr CM, Mukai S, Higashi H, Aikawa M. 2020. The impact of
623 PARPs and ADP-ribosylation on inflammation and host-pathogen interactions. Genes
624 Dev 34:341-359.
625 21. Eriksson KK, Cervantes-Barragan L, Ludewig B, Thiel V. 2008. Mouse hepatitis virus
626 liver pathology is dependent on ADP-ribose-1"-phosphatase, a viral function conserved in
627 the alpha-like supergroup. J Virol 82:12325-34.
628 22. Fehr AR, Athmer J, Channappanavar R, Phillips JM, Meyerholz DK, Perlman S. 2015.
629 The nsp3 macrodomain promotes virulence in mice with coronavirus-induced
630 encephalitis. J Virol 89:1523-36.
631 23. Grunewald ME, Chen Y, Kuny C, Maejima T, Lease R, Ferraris D, Aikawa M, Sullivan
632 CS, Perlman S, Fehr AR. 2019. The coronavirus macrodomain is required to prevent
633 PARP-mediated inhibition of virus replication and enhancement of IFN expression. PLoS
634 Pathog 15:e1007756.
635 24. Alhammad YMO, Fehr AR. 2020. The Viral Macrodomain Counters Host Antiviral
636 ADP-Ribosylation. Viruses 12:384.
637 25. Abraham R, Hauer D, McPherson RL, Utt A, Kirby IT, Cohen MS, Merits A, Leung
638 AKL, Griffin DE. 2018. ADP-ribosyl-binding and hydrolase activities of the alphavirus
639 nsP3 macrodomain are critical for initiation of virus replication. Proc Natl Acad Sci U S
640 A 115:E10457-E10466.
641 26. Abraham R, McPherson RL, Dasovich M, Badiee M, Leung AKL, Griffin DE. 2020.
642 Both ADP-Ribosyl-Binding and Hydrolase Activities of the Alphavirus nsP3
643 Macrodomain Affect Neurovirulence in Mice. mBio 11.

644 27. McPherson RL, Abraham R, Sreekumar E, Ong SE, Cheng SJ, Baxter VK, Kistemaker
645 HA, Filippov DV, Griffin DE, Leung AK. 2017. ADP-ribosylhydrolase activity of
646 Chikungunya virus macrodomain is critical for virus replication and virulence. Proc Natl
647 Acad Sci U S A 114:1666-1671.
648 28. Parvez MK. 2015. The hepatitis E virus ORF1 'X-domain' residues form a putative
649 macrodomain protein/Appr-1"-pase catalytic-site, critical for viral RNA replication. Gene
650 566:47-53.
651 29. Vuksanovic N, Silvaggi, N.R. National Science Foundation (NSF, United States). 2020.
652 High-resolution structure of the SARS-CoV-2 NSP3 Macro X domain doi:
653 10.2210/pdb6WEY/pdb. doi:10.2210/pdb6WEY/pdb.
654 30. Michalska K, Stols, L., Jedrzejczak, R., Endres, M., Babnigg, G., Kim, Y., Joachimiak,
655 A., Center for Structural Genomics of Infectious Diseases (CSGID). 2020. Crystal
656 Structure of ADP ribose phosphatase of NSP3 from SARS-CoV-2 in the apo doi:
657 10.2210/pdb6WEN/pdb. doi:10.2210/pdb6wen/pdb.
658 31. Michalska K, Kim, Y., Jedrzejczak, R., Maltseva, N., Endres, M., Mececar, A.,
659 Joachimiak, A., Center for Structural Genomics of Infectious Diseases (CSGID). 2020.
660 Crystal Structure of ADP ribose phosphatase of NSP3 from SARS CoV-2 in the complex
661 with ADP ribose doi: 10.2210/pdb6W02/pdb. doi:10.2210/pdb6W02/pdb.
662 32. Frick DN, Virdi RS, Vuksanovic N, Dahal N, Silvaggi NR. 2020. Molecular Basis for
663 ADP-Ribose Binding to the Mac1 Domain of SARS-CoV-2 nsp3. Biochemistry (Mosc)
664 59:2608-2615.
665 33. Jankevicius G, Hassler M, Golia B, Rybin V, Zacharias M, Timinszky G, Ladurner AG.
666 2013. A family of macrodomain proteins reverses cellular mono-ADP-ribosylation. Nat
667 Struct Mol Biol 20:508-14.
668 34. Leung AKL, McPherson RL, Griffin DE. 2018. Macrodomain ADP-ribosylhydrolase and
669 the pathogenesis of infectious diseases. PLoS Pathog 14:e1006864.
670 35. Lei J, Kusov Y, Hilgenfeld R. 2018. Nsp3 of coronaviruses: Structures and functions of a
671 large multi-domain protein. Antiviral Res 149:58-74.
672 36. Heer CD, Sanderson DJ, Alhammad YMO, Schmidt MS, Trammell SAJ, Perlman S,
673 Cohen MS, Fehr AR, Brenner C. 2020. Coronavirus and PARP expression dysregulate
674 the NAD Metabolome: a potentially actionable component of innate immunity. bioRxiv
675 doi:10.1101/2020.04.17.047480.
676 37. Shull NP, Spinelli SL, Phizicky EM. 2005. A highly specific phosphatase that acts on
677 ADP-ribose 1"-phosphate, a metabolite of tRNA splicing in Saccharomyces cerevisiae.
678 Nucleic Acids Res 33:650-60.
679 38. Rosenthal F, Feijs KL, Frugier E, Bonalli M, Forst AH, Imhof R, Winkler HC, Fischer D,
680 Caflisch A, Hassa PO, Luscher B, Hottiger MO. 2013. Macrodomain-containing proteins
681 are new mono-ADP-ribosylhydrolases. Nat Struct Mol Biol 20:502-7.
682 39. Sharifi R, Morra R, Appel CD, Tallis M, Chioza B, Jankevicius G, Simpson MA, Matic I,
683 Ozkan E, Golia B, Schellenberg MJ, Weston R, Williams JG, Rossi MN, Galehdari H,
684 Krahn J, Wan A, Trembath RC, Crosby AH, Ahel D, Hay R, Ladurner AG, Timinszky G,
685 Williams RS, Ahel I. 2013. Deficiency of terminal ADP-ribose protein glycohydrolase
686 TARG1/C6orf130 in neurodegenerative disease. EMBO J 32:1225-37.
687 40. Gibson BA, Conrad LB, Huang D, Kraus WL. 2017. Generation and Characterization of
688 Recombinant Antibody-like ADP-Ribose Binding Proteins. Biochemistry (Mosc)
689 56:6305-6316.

690 41. Affar EB, Duriez PJ, Shah RG, Winstall E, Germain M, Boucher C, Bourassa S, Kirkland
691 JB, Poirier GG. 1999. Immunological determination and size characterization of
692 poly(ADP-ribose) synthesized in vitro and in vivo. Biochim Biophys Acta 1428:137-46.
693 42. Asokanathan C, Tierney S, Ball CR, Buckle G, Day A, Tanley S, Bristow A, Markey K,
694 Xing D, Yuen CT. 2018. An ELISA method to estimate the mono ADP-
695 ribosyltransferase activities: e.g in pertussis toxin and vaccines. Anal Biochem 540-
696 541:15-19.
697 43. Langelier MF, Planck JL, Servent KM, Pascal JM. 2011. Purification of human PARP-1
698 and PARP-1 domains from Escherichia coli for structural and biochemical analysis.
699 Methods Mol Biol 780:209-26.
700 44. Wang Z, Gagne JP, Poirier GG, Xu W. 2014. Crystallographic and biochemical analysis
701 of the mouse poly(ADP-ribose) glycohydrolase. PLoS One 9:e86010.
702 45. Kabsch W. 1988. Evaluation of Single-Crystal X-Ray-Diffraction Data from a Position-
703 Sensitive Detector. J Appl Crystallogr 21:916-924.
704 46. Kabsch W. 2010. Xds. Acta Crystallogr D Biol Crystallogr 66:125-32.
705 47. Vonrhein C, Flensburg C, Keller P, Sharff A, Smart O, Paciorek W, Womack T,
706 Bricogne G. 2011. Data processing and analysis with the autoPROC toolbox. Acta
707 Crystallogr D Biol Crystallogr 67:293-302.
708 48. Evans PR. 2011. An introduction to data reduction: space-group determination, scaling
709 and intensity statistics. Acta Crystallogr D Biol Crystallogr 67:282-92.
710 49. McCoy AJ, Grosse-Kunstleve RW, Adams PD, Winn MD, Storoni LC, Read RJ. 2007.
711 Phaser crystallographic software. J Appl Crystallogr 40:658-674.
712 50. Adams PD, Afonine PV, Bunkoczi G, Chen VB, Davis IW, Echols N, Headd JJ, Hung
713 LW, Kapral GJ, Grosse-Kunstleve RW, McCoy AJ, Moriarty NW, Oeffner R, Read RJ,
714 Richardson DC, Richardson JS, Terwilliger TC, Zwart PH. 2010. PHENIX: a
715 comprehensive Python-based system for macromolecular structure solution. Acta
716 Crystallogr D Biol Crystallogr 66:213-21.
717 51. Emsley P, Lohkamp B, Scott WG, Cowtan K. 2010. Features and development of Coot.
718 Acta Crystallogr D Biol Crystallogr 66:486-501.
719 52. Chen VB, Arendall WB, 3rd, Headd JJ, Keedy DA, Immormino RM, Kapral GJ, Murray
720 LW, Richardson JS, Richardson DC. 2010. MolProbity: all-atom structure validation for
721 macromolecular crystallography. Acta Crystallogr D Biol Crystallogr 66:12-21.
722 53. Potterton L, McNicholas S, Krissinel E, Gruber J, Cowtan K, Emsley P, Murshudov GN,
723 Cohen S, Perrakis A, Noble M. 2004. Developments in the CCP4 molecular-graphics
724 project. Acta Crystallogr D Biol Crystallogr 60:2288-94.
725 54. Krissinel E. 2012. Enhanced fold recognition using efficient short fragment clustering. J
726 Mol Biochem 1:76-85.
727 55. Evans P. 2006. Scaling and assessment of data quality. Acta Crystallogr D Biol
728 Crystallogr 62:72-82.
729 56. Diederichs K, Karplus PA. 1997. Improved R-factors for diffraction data analysis in
730 macromolecular crystallography. Nat Struct Biol 4:269-75.
731 57. Weiss MS. 2001. Global indicators of X-ray data quality. J Appl Crystallogr 34:130-135.
732 58. Evans P. 2012. Resolving some old problems in protein crystallography. Science
733 336:986-7.
734 59. Karplus PA, Diederichs K. 2012. Linking crystallographic model and data quality.
735 Science 336:1030-3.

736
737 **FIGURE LEGENDS**

738 **Figure 1.** The SARS-CoV-2 Mac1 is a small domain within nsp3 and is highly conserved
739 between other human CoV Mac1 protein domains. (A) Cartoon Schematic of the SARS-CoV-2
740 non-structural protein 3. The conserved macrodomain, or Mac1, is highlighted in yellow. (B)
741 Sequence alignment of Mac1 from CoVs; SARS-CoV-2, SARS-CoV, MERS-CoV, and mouse
742 hepatitis virus (MHV), and from alphaviruses Venezuelan equine encephalitis virus (VEEV) and
743 sindbis virus (SINV), and hepatitis E virus (HEV). Sequences were aligned using the ClustalW
744 method from Clustal Omega online tool with manual adjustment. Identical residues are bolded,
745 shaded in grey, and marked with asterisks; semiconserved residues were shaded in grey and
746 marked with two dots (one change amongst all viruses) or one dot (2 changes or conserved
747 within CoV family).

748 **Figure 2.** Structure of SARS-CoV-2 Mac1 complexed with ADP-ribose. **A)** The structure was
749 rendered as a blend through model from the N-terminus (blue) to the C-terminus (red). **B)** The
750 structure was colored by secondary structure showing sheets (magenta) and helices (green). The
751 ADP-ribose is rendered as gray cylinders with oxygens and nitrogens colored red and blue,
752 respectively.

753 **Figure 3.** Binding mode of ADP-ribose in SARS-CoV-2 Mac1. **A)** Fo-Fc Polder omit map
754 (green mesh) contoured at 3σ. **B)** Hydrogen bond interactions (dashed lines) between ADP-
755 ribose and amino acids. **C)** Interactions with water molecules. Direct hydrogen bond interactions
756 are represented by dashed lines and water mediated contacts to amino acids are drawn as solid
757 lines.

758 **Figure 4**. Structural comparison of the SARS-CoV-2 Mac1 protein with the SARS-CoV and
759 MERS-CoV Mac1 proteins. **A-B)** Superposition of SARS-CoV-2 macrodomain (magenta) with

760 coronavirus macrodomain structures. **A**) SARS-CoV Mac1 with ADP-ribose (gold) (2FAV) and
761 **B**) MERS-CoV Mac1 with ADP-ribose (teal) (5HOL). **C-D)** Superposition of SARS-CoV-2
762 Mac1 (magenta) with other coronavirus Mac1 structures highlighting the ADP-ribose binding
763 site. **C**) SARS-CoV (gold), **D**) MERS-CoV (teal). The ADP-ribose molecules are colored gray
764 for SARS-CoV-2 Mac1 (**A-D**) and are rendered as green cylinders for SARS-CoV Mac1 (panel
765 **A,C**) and MERS-CoV Mac1 (panel **B,D**).
766 **Figure 5**. Human CoVs bind to ADP-ribose with similar affinity. **A-B)** ADP-ribose binding of
767 human Mdo2 and SARS-CoV, MERS-CoV, and SARS-CoV-2 Mac1 proteins by ITC. Images in
768 **(A)** are of one experiment representative of at least 2 independent experiments. Data in **(B)**
769 represent the combined averages of multiple independent experiments for each protein. Mdo2
770 n=2; SARS-CoV n=5; MERS-CoV n=6; SARS-CoV-2 n=2.
771 **Figure 6**. Coronavirus Mac1 proteins are ADP-ribosylhydrolases. **A)** The SARS-CoV-2
772 macrodomain was incubated with MARylated PARP10 CD *in vitro* at equimolar ratios (1 μM)
773 for the indicated times at 37°C. ADP-ribosylated PARP10 CD was detected by immunoblot (IB)
774 with anti-ADP-ribose binding reagent (Millipore-Sigma MAB1076). Total PARP10 CD and
775 macrodomain protein levels were determined by Coomassie Blue (CB) staining. PARP10 CD
776 incubated alone at 37°C was stopped at 0 or 60 minutes. **B)** The level of de-MARylation was
777 measured by quantifying band intensity using Image J software. Intensity values were plotted
778 and fit to a non-linear regression curve with error bars representing standard deviation. Results in
779 **A** are representative experiments of two independent experiments and data in **B** represent the
780 combined results of the two independent experiments. **C)** The Mdo2, MERS-CoV, SARS-CoV,
781 and SARS-CoV-2 macrodomains were incubated with MARylated PARP10 CD *in vitro* at the
782 following ratios of [substrate]:[Mac1]: 1:1 (1 μM), 5:1 (500 nM, 100 nM), or 10:1 (1 μM, 100

783 nM) for the indicated times at 37°C. ADP-ribosylated PARP10 CD was detected as described
784 above, and total PARP10 CD and macrodomain protein levels were determine by Coomassie
785 Blue (Fig. S6). **D)** Time-dependent substrate concentrations were determined by quantifying
786 band intensity using Image Studio software. The data were then analyzed using Mathematica 12,
787 as described in Methods, to determine the initial rate (*k*) of substrate decay. Results in **C** are
788 representative experiments of three independent experiments and data in **D** represent the
789 combined results of the three independent experiments.
790 **Fig. 7.** Coronavirus Mac1 proteins do not hydrolyze PAR. PAR hydrolase assays were performed
791 with PARP1 either extensively poly-ADP-ribosylated (500 μM NAD^+) or partially poly-ADP-
792 ribosylated (5 μM NAD^+) to produce oligo-ADP-ribose. Macrodomains were incubated with
793 both automodified PARP1 substrates for 1 hour. PAR was detected by immunoblot with the anti-
794 PAR antibody 96-10. PARG (catalytically active 60 kD fragment) was used as a positive control.
795 The results are representative of 2 independent experiments.
796 **Figure 8.** Development of an ELISA assay to detect de-MARylation. **A)** Cartoon schematic of
797 the ELISA assay. ELISA plates pre-coated with glutathione and pre-blocked were used capture
798 GST-tagged PARP10 proteins, which was used as a substrate for de-MARylation. The removal
799 of MAR was detected by anti-MAR antibodies. **B)** MARylated PARP10 (MAR+) and non-
800 MARylated PARP10 (MAR-) with no SARS-CoV-2 Mac1 as controls were detected with anti-
801 mono-ADP-ribose binding reagent (α-MAR) (Millipore-Sigma MAB1076) or with anti-GST (α-
802 GST) (Invitrogen, MA4-004). **C)** Starting at 12.5 nM, 2-fold serial dilutions of the SARS-CoV-2
803 Mac1 protein was incubated in individual wells with MARylated PARP10-CD for 60 min at
804 37°C**.** The graph represents the combined results of 2 independent experiments.
805

806 **SUPPLEMENTAL FIGURE LEGENDS**

807 **Figure S1**. Purification and crystallization of macrodomain proteins. **A)** Macrodomain proteins
808 were purified as described in Methods. Equimolar amounts of the recombinant proteins were run
809 on a polyacrylamide gel and visualized by Coomassie staining. **B)** Crystals of SARS-CoV-2
810 Mac1 obtained with Salt Rx HT E10 supplemented with 0.1 M NDSB-256.

811 **Figure S2.** Extended residues at the C-terminus of the SARS-CoV-2 Mac1 clashed with
812 symmetry related molecules. **A)** Comparison of the amino acid sequence of SARS-CoV-2 Mac1,
813 6W02 and 6WEY. **B)** Superposition of SARS-CoV-2 Mac1 (magenta) subunit B onto subunit A
814 of 6W02 reveals that the C-terminus would clash with symmetry related molecules (coral).

815 **Figure S3**. Comparison of the SARS-CoV-2 Mac1 protein with homologous structures. **A-B)**
816 Superposition of SARS-CoV-2 Mac1 (magenta) with other recently determined homologous
817 structures. **A)** SARS-CoV-2 Mac1 apo structure (6WEN), **B)** SARS-CoV-2 Mac1 complexed
818 with ADP-ribose (6W02). The ADP-ribose molecule is colored gray for SARS-CoV-2 and is
819 represented as green cylinders for 6W02 in panel **B**. **C-D)** Comparison of the residues in the
820 ADP-ribose binding site. **C**) SARS-CoV-2 Mac1 apo structure (blue, 6WEN), **D**) SARS-CoV-2
821 Mac1 complexed with ADP-ribose (green, 6W02). The ADP-ribose of SARS-CoV-2 is rendered
822 as gray cylinders, and is represented as green cylinders for 6W02 in panel **B**.

823 **Figure S4**. ADP-ribose binding of macrodomain proteins by DSF assay. The macrodomain
824 proteins (10 μM) were incubated with increasing concentrations of ADP-ribose and measured by
825 DSF as described in Methods. Mdo2 n=4; SARS-CoV n=6; MERS-CoV n=5; SARS-CoV-2 n=3.

826 **Figure S5**. Affinity of ADP-ribose binding antibodies for ADP-ribosylated PARP10 CD.
827 MARylated PARP10 and non-MARylated PARP10 CD were detected by immunoblot (IB) with
828 anti-GST (Invitrogen, MA4-004), anti-ADP-ribose binding reagents: anti-MAR (Millipore-

829 Sigma MAB1076), anti-PAR (Millipore-Sigma MABC547), and anti-MAR/PAR (Millipore-
830 Sigma MABE1075) antibodies.
831 **Figure S6.** MARylated PARP10 stability over time. The presence of mono-ADP-ribose of
832 automodified PARP10 without any macrodomain was detected at 6 time points by immunoblot
833 analysis with the anti-GST (Invitrogen, MA4-004) and anti-ADP-ribose binding reagent anti-
834 MAR (Millipore-Sigma MAB1076).
835 **Figure S7.** The CoVs and human Mdo2 macrodomain proteins were incubated with MARylated
836 PARP10 CD *in vitro* for the indicated times at 37°C. Total PARP10 CD and macrodomain
837 protein levels were determined by Coomassie Blue (CB) staining. Results showone experiment
838 of three independent experiments.
839 **Figure S8**. Differential PARylation of PARP1 by varying concentrations of NAD^+. Recombinant
840 human PARP1 was automodified in a reaction buffer supplemented with increasing
841 concentrations of NAD^+ to generate substrates for the PAR hydrolase assays. PAR was detected
842 by immunoblot analysis of reaction products with the anti-PAR antibody 96-10.

A

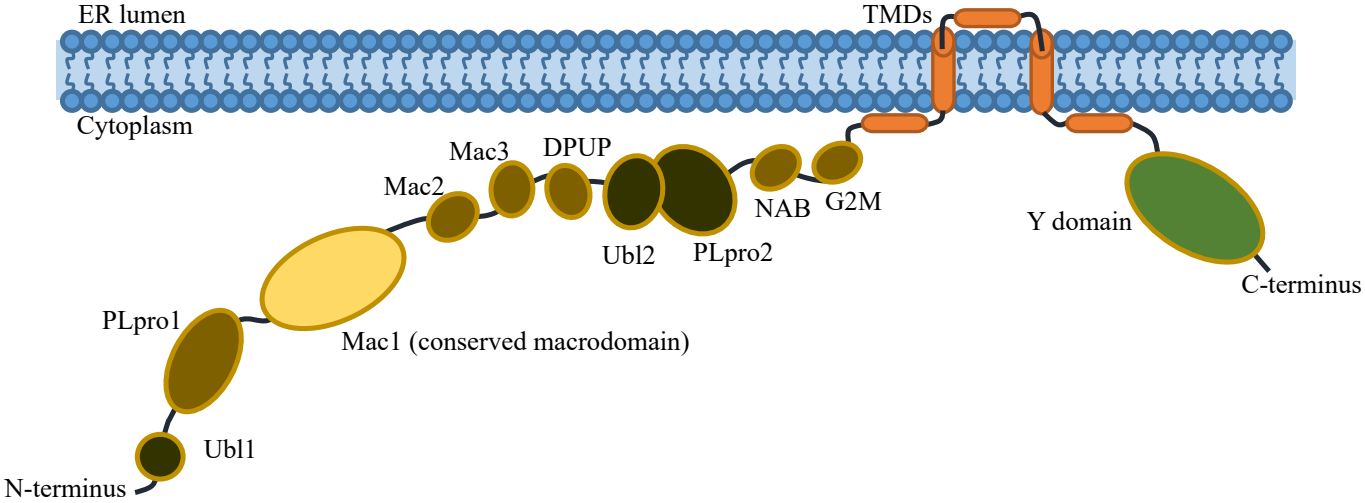

B

```
SARS-CoV-2 aa          10            20        30        40        50        60        70
                        |             |         |         |         |         |         |
SARS-CoV-2   IEVNSFSGYLKLT-----DNVYIKNADIVEEAKKVKPTVVVNAANVYLKHGGGVAGALNKATNNAMQVESDDYIATNGP  74
SARS-CoV     EPVNQFTGYLKLT-----DNVAIKCVDIVKEAQSANPMVIVNAANIHLKHGGGVAGALNKATNGAMQKESDDYIKLNGP  74
MERS-CoV     -PLSNFEH-KVIT-----ECVTIVLGDAIQVAKCYGESVLVNAANTHLKHGGGIAGAINAASKGAVQKESDEYILAKGP  72
MHV          -----LYG-SCIT-----PNVCFVKGDVIKVLRRVGAEVIVNPANGRMAHGAGVAGAIAKAAGKAFINETADMVKAQGV  68
VEEV         -----YTG-SRLHEAGCAPSYHVVRGDI----ATATEGVIINAANSKGQPGGGVCGALYKKFPESFDLQPIE-------  62
SINV         -----------------APSYRTKRENI----ADCQEEAVVNAANPLGRPGEGVCRAIYKRWPNSFTDSATE-------  51
HEV          ----------------YPDGSKVFAGSL----FESTCTWLVNASNVDHRPGGGLCHAFYQRYPASFDAASFVMR-----  54
Conservation              .       .     .           . :*::*     * * ..        .   .

SARS-CoV-2 a.a.   80        90        100         110             120       130         140
                   |         |         |           |               |         |           |
SARS-CoV-2   LKVGGSCVLSGHNLAKHCLHVVGPNVNK--G-EDIQLLKSAYEVF------NQHEVLLAPLLSAGIFGADPIH---SLR  141
SARS-CoV     LTVGGSCLLSGHNLAKKCLHVVGPNLNA--G-EDIQLLKAAYENF------NSQDILLAPLLSAGIFGAKPLQ---SLQ  141
MERS-CoV     LQVGDSVLLQGHSLAKNILHVVGPDARA--K-QDVSLLSKCYKAM------NAYPLVVTPLVSAGIFGVKPAV---SFD  139
MHV          CQVGGCYESTGGKLCKKVLNIVGPDARGHGK-QCYSLLERAYQHI------NKCDNVVTTLISAGIFSVPTDV---SLT  137
VEEV         --VGKARLVK--GVTKHIIHAVGPNFNKVSEVEGDKQLAEAYESIAKIVNDNNYKSVAIPLLSTGIFSGNKDRLTQSLN  137
SINV         --TGTAKLTV--CQGKKVIHAVGPDFRKHPEAEALKLLQNAYHAVADLVNEHNIKSVAIPLLSTGIYAAGKDRLEVSLN  126
HEV          --DGAAAY---TLTPRPIIHAVAPDYRL--E-HNPKRLEAAYRETC-----SRLGTAAYPLLGTGIYQVPIGP---SFD  117
Conservation   .*           .  .: *:*            .*  :*         .       :* :.**.         *.

SARS-CoV-2 a.a.        150       160
                        |         |
SARS-CoV-2   VC---VDTVRTNVYLAVFDKNLYDKLV---------------- 165
SARS-CoV     VC---VQTVRTQVYIAVNDKALYEQVVMDYLDNL--------- 172
MERS-CoV     YL---IREAKTRVLVVVNSQDVYKSLTIVDIPQLE-------- 171
MHV          YL---LGVVTKNVILVSNNQDDFDVIEKCQVTSVAGTK----- 172
VEEV         HLLTALDTTDADVAIYCRDKKWEMT------------------ 162
SINV         CLTTALDRTDADVTIYCLDKKWKERI--DAVLQLKE------- 160
HEV          AWER-NHRPGDELYLPELAARWFEANRPTRPTLIITEDVARTA 159
Conservation              :
```

A

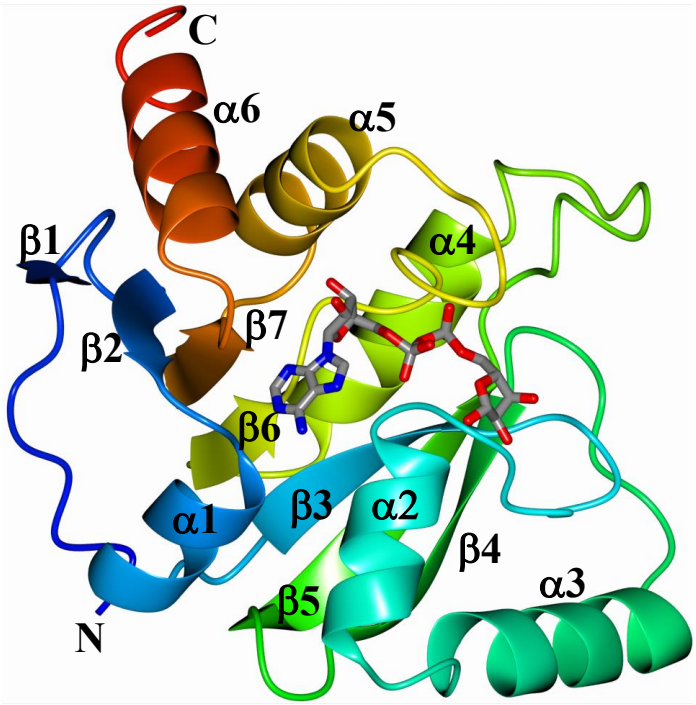

β1: L10-K11
β2: V16-A21
α1: I23-V30
β3: V34-A39
α2: V49-T57
α3: A60-N72
β4: S79-G85
β5: A89-V96
α4: L108-Q118
β6: V121-A124
α5: P136-T146
β7: N150-V155
α6: K158-F168

B

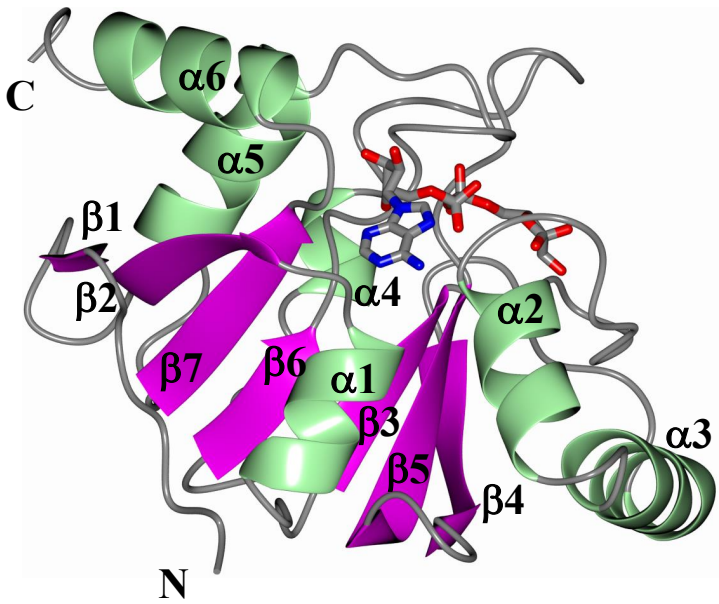

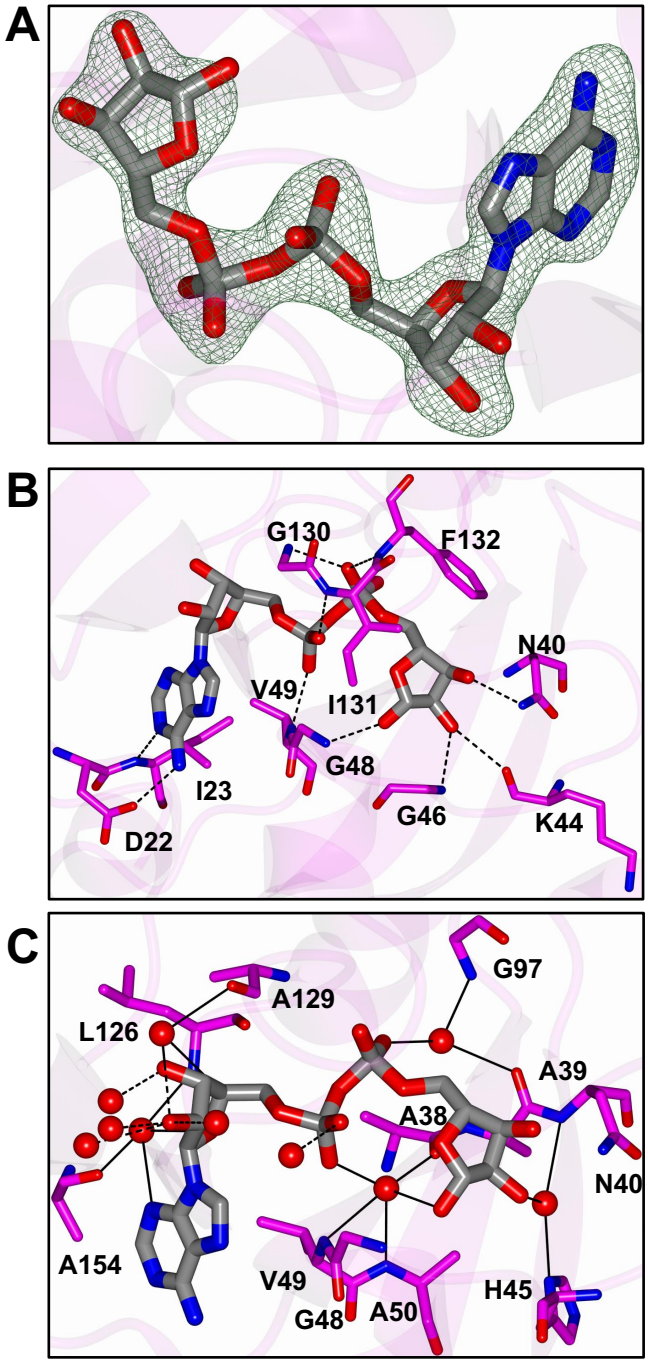
A
B
G130
F132
N40
V49
I131
G48
I23
G46
K44
D22
C
G97
A129
L126
A39
A38
N40
A154
V49
H45
G48
A50

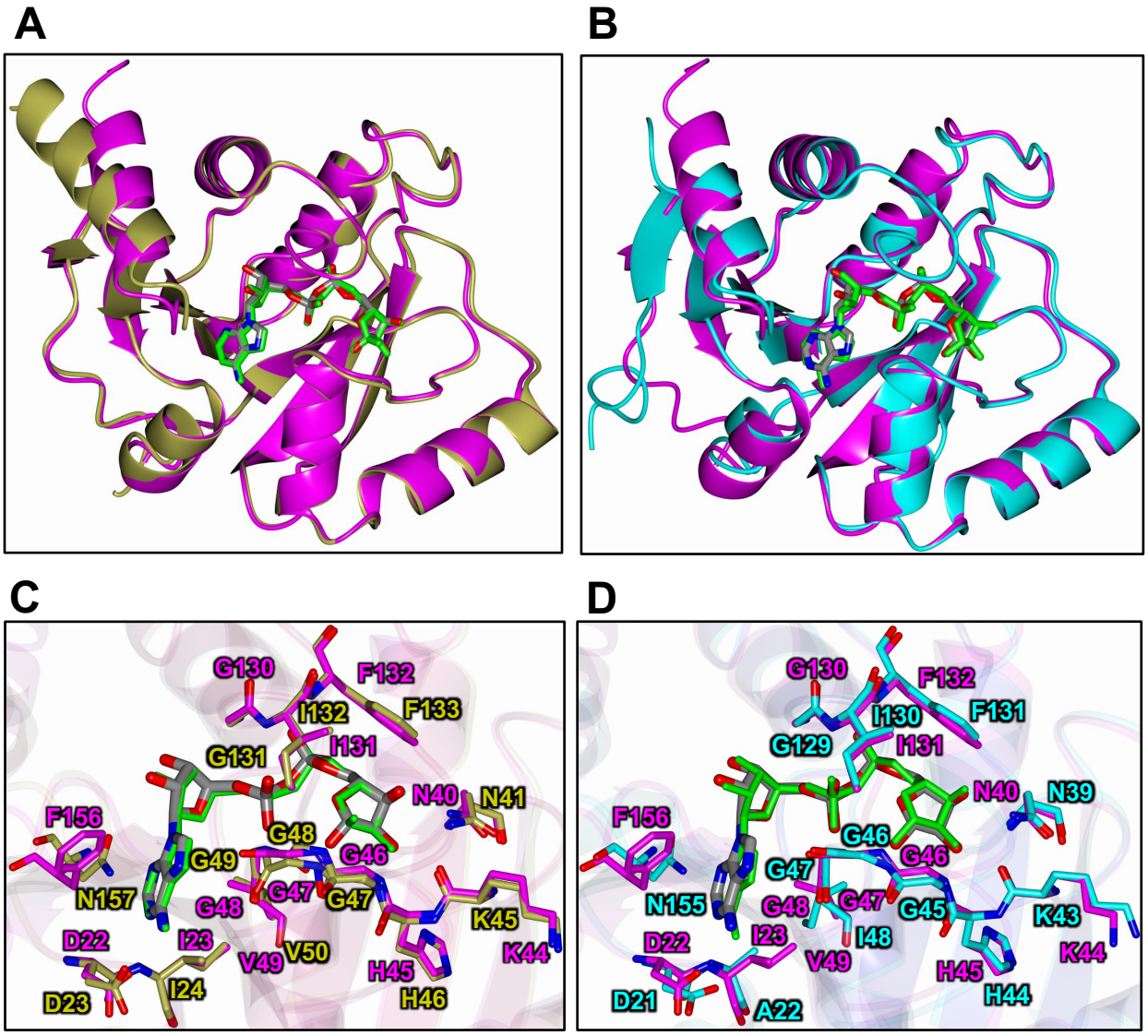
A
B
C
G130
F132
I132
F133
G131
I131
N40
N41
F156
G48
G49
G46
N157
G47
G47
G48
K45
D22
I23
V49
V50
K44
H45
D23
I24
H46
D
G130
F132
I130
F131
G129
I131
N40
N39
F156
G46
G46
G47
N155
G48
G47
G45
K43
D22
I23
I48
V49
K44
H45
D21
A22
H44

A

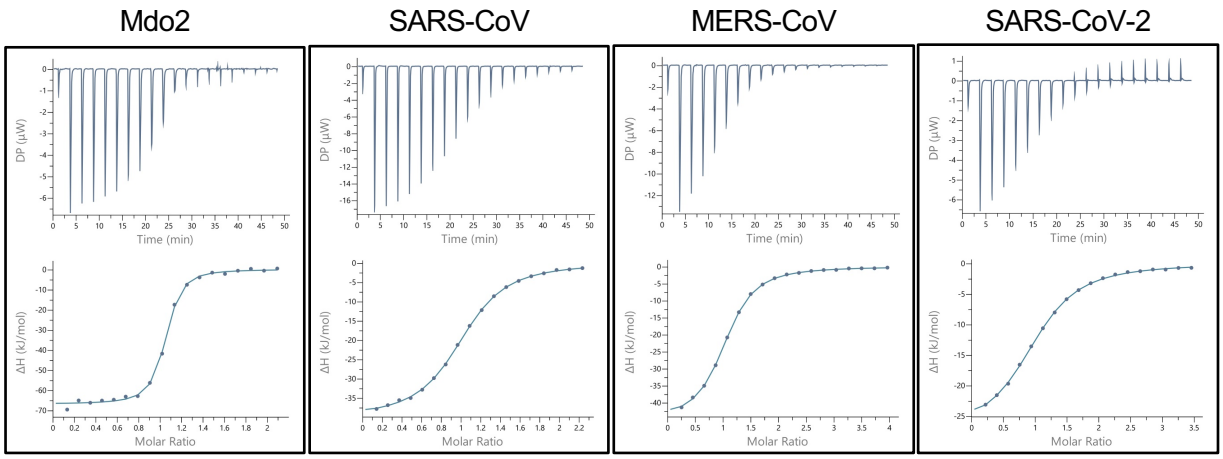

B

Macrodomain	Stoichiometry (N)	Kd (µM)	ΔH (kcal/mol)	ΔG (kcal/mol)
Mdo2	0.92 ± 0.01	0.24 ± 0.02	-66 ± 1	-38 ± 2
SARS-CoV	0.89 ± 0.04	10.8 ± 1.7	-40 ± 1.2	-28 ± 0.4
MERS-CoV	0.97 ± 0.04	7.9 ± 0.15	-47 ± 3	-29 ± 0.4
SARS-CoV-2	1.14 ± 0.06	16.8 ± 0.04	-28 ± 0.1	-27 ± 0.1

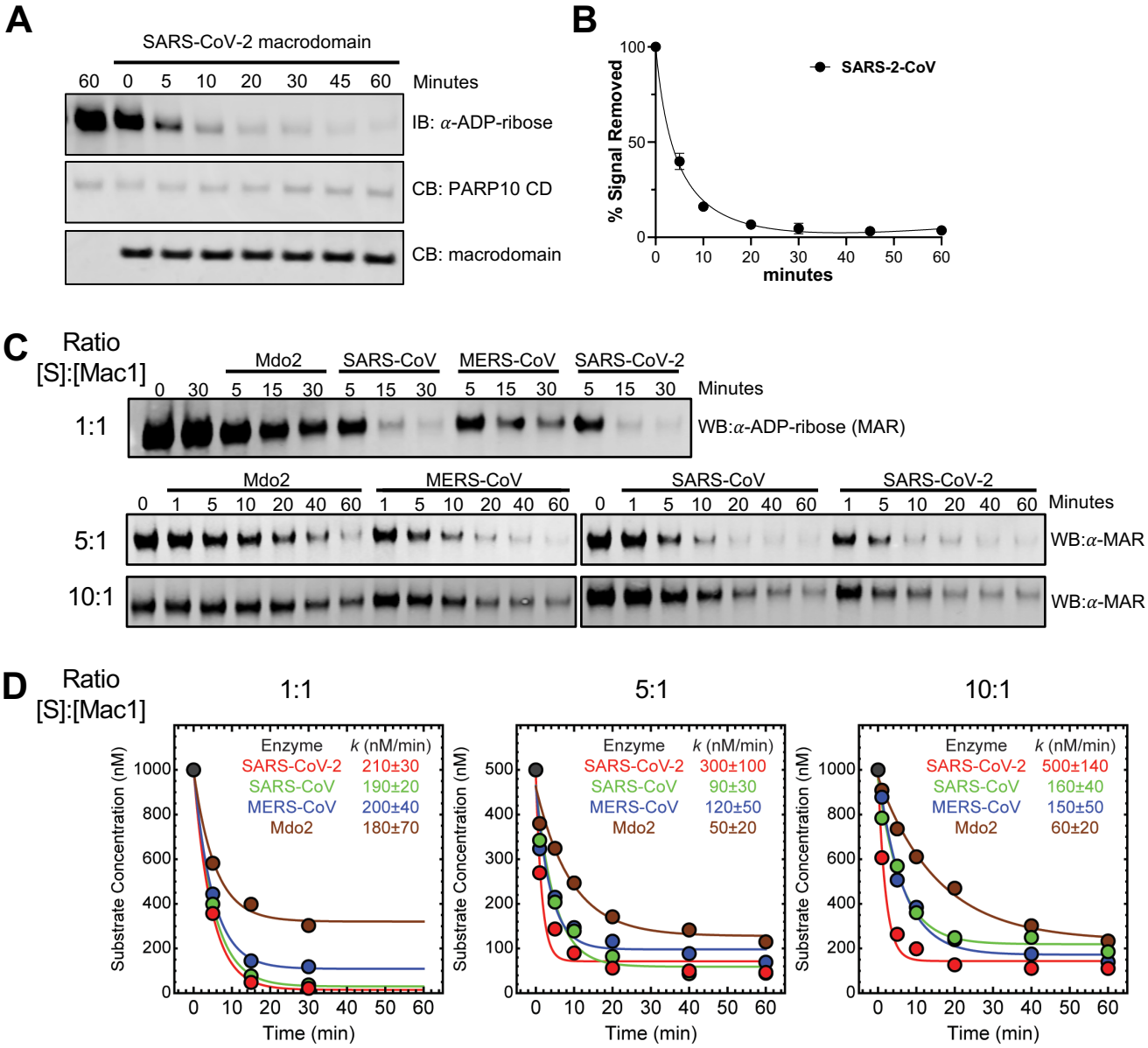
A
SARS-CoV-2 macrodomain
60 0 5 10 20 30 45 60 Minutes
IB: α-ADP-ribose
CB: PARP10 CD
CB: macrodomain
B
SARS-2-CoV
% Signal Removed
minutes
C
Ratio [S]:[Mac1]
Mdo2
SARS-CoV
MERS-CoV
SARS-CoV-2
0 30 5 15 30 5 15 30 5 15 30 5 15 30 Minutes
1:1
WB:α-ADP-ribose (MAR)
0 1 5 10 20 40 60 1 5 10 20 40 60 0 1 5 10 20 40 60 1 5 10 20 40 60 Minutes
5:1
10:1
WB:α-MAR
D
Ratio [S]:[Mac1]
1:1
5:1
10:1
Enzyme k (nM/min)
SARS-CoV-2 210±30
SARS-CoV 190±20
MERS-CoV 200±40
Mdo2 180±70
SARS-CoV-2 300±100
SARS-CoV 90±30
MERS-CoV 120±50
Mdo2 50±20
SARS-CoV-2 500±140
SARS-CoV 160±40
MERS-CoV 150±50
Mdo2 60±20
Substrate Concentration (nM)
Time (min)

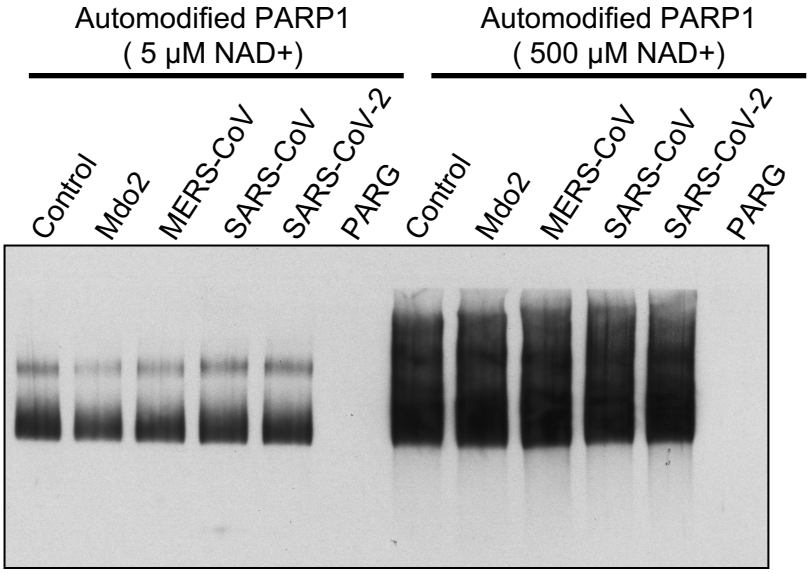
Automodified PARP1
(5 μM NAD+)
Automodified PARP1
(500 μM NAD+)
Control
Mdo2
MERS-CoV
SARS-CoV
SARS-CoV-2
PARG
Control
Mdo2
MERS-CoV
SARS-CoV
SARS-CoV-2
PARG

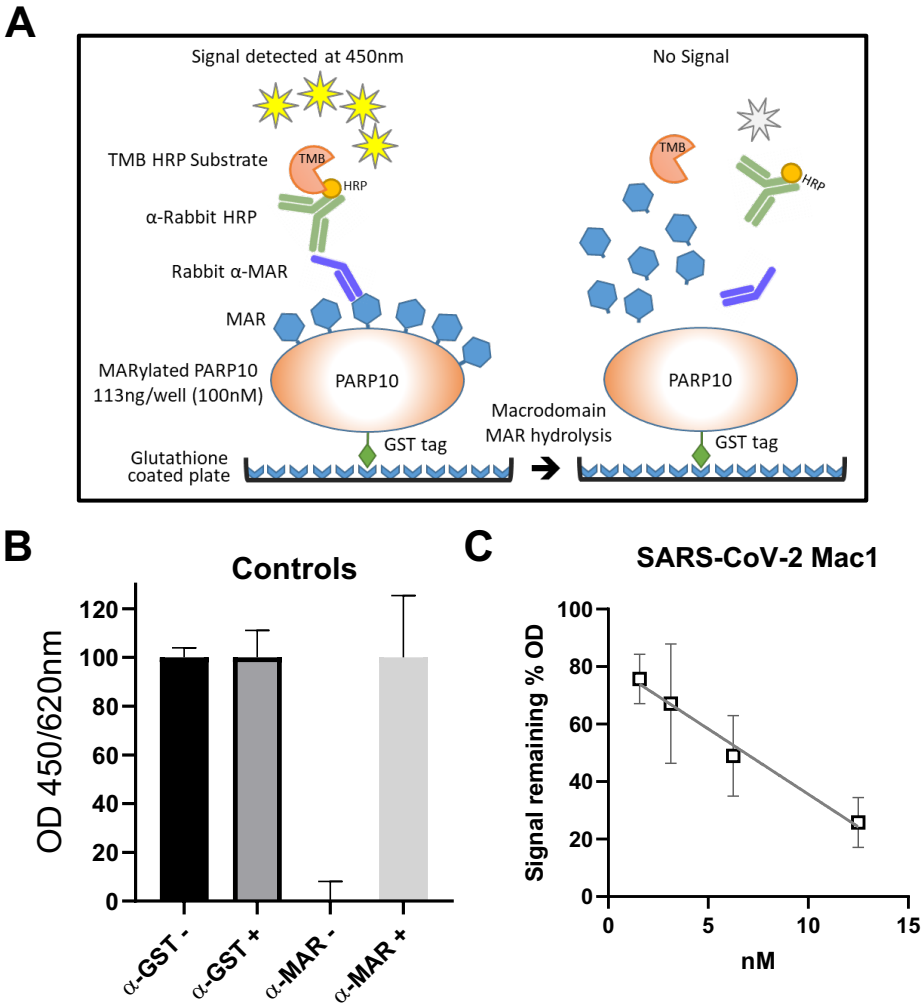
A
Signal detected at 450nm
No Signal
TMB HRP Substrate
TMB
HRP
α-Rabbit HRP
Rabbit α-MAR
MAR
MARylated PARP10
113ng/well (100nM)
PARP10
GST tag
Glutathione
coated plate
Macrodomain
MAR hydrolysis
B
Controls
OD 450/620nm
120
100
80
60
40
20
0
α-GST -
α-GST +
α-MAR -
α-MAR +
C
SARS-CoV-2 Mac1
Signal remaining % OD
100
80
60
40
20
0
0
5
10
15
nM